In-situ microstructural investigations of the TRIP-to-TWIP evolution in Ti-Mo-Zr alloys as a function of Zr concentration

Bingnan Qian, Jinyong Zhang, Yangyang Fu, Fan Sun, Yuan Wu, Jun Cheng, Philippe Vermaut, Frédéric Prima

Research Article

In-situ microstructural investigations of the TRIP-to-TWIP evolution in Ti-Mo-Zr alloys as a function of Zr concentration

Bingnan Qian [1, a], Jinyong Zhang [2, 3, a], Yangyang Fu [2], Fan Sun [1*], Yuan Wu [4], Jun Cheng[3, 5], Philippe Vermaut [1, 6] and Frédéric Prima [1]

[1] *Chimie ParisTech, PSL University, CNRS, Institut de Recherche de Chimie Paris, 75005 Paris, France*

[2] *School of Material Science and Engineering, China University of Mining and Technology, Xuzhou, Jiangsu 221008, China*

[3] *State Key Laboratory of Solidification Processing, Northwestern Polytechnical University, Xi'an, Shaanxi 710072, China*

[4] *State Key Laboratory for Advanced Metals and Materials, University of Science and Technology Beijing, Beijing 100083, China*

[5] *Northwest Institute for Non-ferrous Metal Research, Shaanxi Key Laboratory of Biomedical Metal Materials, Xi'an 710016, China*

[6] *Sorbonne Universities, UPMC University Paris, UFR926, 75005 Paris, France*

[Received 19 March 2020; Received in revised form 5 April 2020; Accepted 7 April 2020]

[a] The authors contributed equally to this work.

* Corresponding author.

E-mail address: fan.sun@chimieparistech.psl.eu (Fan Sun)

Aiming at overcoming the strength-ductility trade-off in structural Ti-alloys, a new family of TRIP/TWIP Ti-alloys was developed in the past decade (TWIP: twinning-induced plasticity; TRIP: transformation-induced plasticity). Herein, we study the tunable nature of deformation mechanisms with various TWIP and TRIP contributions by fine adjustment of the Zr content on ternary Ti-12Mo-xZr (x=3, 6, 10) alloys. The microstructure and deformation mechanisms of the Ti-Mo-Zr alloys are explored by using in-situ electron backscatter diffraction (EBSD) and transmission electron microscopy (TEM). The results show that a transition of the dominant deformation mode occurred, going from TRIP to TWIP major mechanism with increasing Zr content. In the Ti-12Mo-3Zr alloy, the stress-induced martensitic transformation (SIM) is the major deformation mode which accommodates the plastic flow. Regarding the Ti-12Mo-6Zr alloy, the combined deformation twinning (DT) and

SIM modes both contribute to the overall plasticity with enhanced strain-hardening rate and subsequent large uniform ductility. Further increase of the Zr content in Ti-12Mo-10Zr alloy leads to an improved yield stress involving single DT mode as a dominant deformation mechanism throughout the plastic regime. In the present work, a set of comprehensive in-situ and ex-situ microstructural investigations clarify the evolution of deformation microstructures during tensile loading and unloading processes.
Keywords: Metastable beta (β) Ti-alloys; TRIP/TWIP effects; Deformation mechanisms; in-situ traction-EBSD; TEM observation.

1. Introduction

Titanium and its alloys have attracted much attention due to their high strength [1, 2], low density [3], excellent properties of biocompatibility, and good corrosion resistance [1, 4, 5]. However, compared to traditional structural alloys, such as stainless steel and Co-Cr alloys, their low ductility and the lack of strain-hardening limited their applications where combination of strength and ductility are required. Recently, combination of high strength, large ductility, and excellent strain-hardening rate has been achieved in a new family of metastable β titanium alloys, such as Ti-12Mo [6], Ti-9Mo-6W[7], Ti-6Cr-4Mo-2Al-2Sn-1Zr [8], Ti-12Mo-5Zr [9], Ti-11Mo-5Sn-5Nb [10] and Ti-18Zr-13Mo [11], with TWIP and/or TRIP effects, leading to greater potential applications. Recent studies have reported complex deformation mechanisms mainly involving deformation twinning ({332}<113> mode and {112}<111> mode) and stress-induced martensite (SIM α″), in addition to dislocation slip. As a result of these simultaneously activated mechanisms, a high strain-hardening rate may be reached by a microstructural evolution during plastic flow. This microstructural evolution has been shown to give birth to: (1) the so-called dynamic Hall-Petch effect [12, 13]; (2) a strong mechanical contrast effect between the twins and their matrix due to high elastic anisotropy of BCC β phase in titanium alloys [14]; (3) a dense multi-modal twinning network [11]; (4) a hierarchical twin/SIM α″ microstructure [6, 7, 13, 15, 16].

As well-known, the TRIP and TWIP effects and their influence on mechanical properties are highly dependent on the stability of β phase in Ti-alloys. Martensitic transformation (β → α″) can be favorably activated by applying external stress or strain in the β-metastable Ti-alloys when the chemical stability of β phase (usually estimated by Mo-equivalent content, Mo_{eq} wt.%) is relatively low at a rough range of 10.0% ≤ alloy Mo_{eq} ≤ 13% [17, 18]. Mechanical twinning can be mainly activated when the β stability becomes higher (Mo_{eq} roughly between 12% and 15%) [6, 19, 20]. For

alloys displaying intermediate β stability (overlapping zone between the two ranges), the simultaneous occurrence of TRIP/TWIP effects has been observed [6, 7]. Therefore, a continuous transition of deformation mechanisms, from near-TRIP to near-TWIP effects, can be expected by increasing progressively the chemical stability of a TRIP/TWIP alloy.

The Zr element has been found to be a neutral element (in Ti-Zr system) or weak β-stabilizing element (in Ti-Nb-Zr system) [21, 22]. Previous studies have reported that the nature of Zr in a Ti-M-Zr system (M = β-stabilizer alloying element) strongly depends on the β-stability and concentration of M [9, 21, 22]. A theoretical equivalence factor of Zr in the Mo_{eq} estimation has been proposed to be +0.47 by Wang et al. [23], showing that the β stabilizing effect of Zr is about half of that of Mo. Therefore, using Zr could be two-fold advantageous since a wide composition range (up to tens of weight percent) can be added into the master alloy: (1) to achieve better tolerance of alloys composition for TRIP/TWIP fine-tuning; (2) to obtain the solution strengthening effect. Furthermore, the exact effect of different Zr additions in the TRIP/TWIP Ti-Mo system has not yet been reported with systematical experimental results. In order to study the effect of Zr addition on the TRIP to TWIP transition in Ti-Mo system, a comparative investigation is performed between the TRIP/TWIP Ti-12Mo-xZr (x= 3, 6, 10) (wt. %) alloys. This work focuses on in-situ investigations of the deformation mechanisms in β phase with different stability levels. The investigation is performed at various length scales using the Ti-12Mo-xZr system. The deformation sequence, orientation relationships and the volume fraction of SIM α″ at different strain levels are traced by in-situ EBSD analysis during tensile loading and after unloading. The in-situ observations reveal the details of the formation, development and transformation of the complex martensite/twin structure. Based on the results, the deformation mechanisms involved in the macroscopic mechanical behavior are discussed by considering the heterogeneous nature of the microstructural evolution.

2. Experimental

100g ingots of Ti-12Mo-xZr were fabricated by vacuum arc-melting using high purity Ti, Mo and Zr elements. These alloys were melted at least five times under a high purity argon atmosphere. The ingots were annealed in vacuum tubular furnace under 2.0×10^{-4} Pa at 1173K for 1.8 ks, followed by water-quenching. The quenched ingots were cold-rolled to 0.5mm sheets, corresponding to reduction rate of 95%. The cold-rolled sheets were solution-treated at 1173K under high vacuum (2.0×10^{-4} Pa) for 1.8 ks and then water-quenched to retain the fully recrystallized β microstructure. Tensile tests were conducted by using an INSTRON 5982 machine

at room temperature with an initial strain rate of $10^{-3}s^{-1}$. Phase characterization was carried out by X-ray diffraction (XRD) using Bruker D8 ADVANCE with CuKα radiation operating at 40 kV and 40 mA. Deformation microstructures were analyzed by using in-situ tensile tests coupled with electron backscatter diffraction (EBSD) scans, performed on a Proxima 100-Micromecha machine in a field emission gun scanning electron microscope (FEG-SEM ZEISS LEO1530) operating at 20 kV and a NORDIF EBSD camera. A JEOL 2100plus transmission electron microscope (TEM) operating at 200 kV was used to carry out fine-scale microstructure analysis. Samples for TEM observations were prepared by a twin-jet polishing technique, using a solution of 4% perchloric acid in methanol, held at about 250 K.

3. Results

3.1 Characterization of solution treated (ST) states

Fig. 1 shows the XRD profiles, optical micrographs and selected-area electron diffraction (SAED) patterns of the ST samples of Ti-12Mo-3Zr, Ti-12Mo-6Zr, and Ti-12Mo-10Zr alloys, respectively. As shown in Fig. 1(a), the presence of the β phase is confirmed in the three alloys without other additional diffraction peaks. It can be noticed that the peak position of the β phase (2θ: degree) slightly shifts towards lower angles with the increasing of Zr content, suggesting a small expansion of the β phase lattice parameter consistent with the bigger size of Zr atoms. Fig. 1(b) displays that the microstructure of ST samples consists in typical recrystallized β grains (with a grain size in the range 50-80 μm). Moreover, besides the β phase, the nanometer athermal ω (ω_{ath}) phase is actually detected by TEM technique, as displayed in Fig. 1(c). It can be observed that the reflections of ω_{ath} phase become weaker and more diffuse with the increased Zr content, when normalized to the β matrix reflection intensities, suggesting that the ω_{ath} precipitation could probably be lower in volume fraction. Pang et al. [24] has observed that Zr addition in Ti-24Nb-[0-8]Zr (at.%) alloys could suppress the formation of ω phase. In contrast to the results of Pang et al [24], the reflections of ω_{ath} phase is still visible in Ti-12Mo-10Zr alloy.

3.2 Tensile properties

Fig. 2 shows the true strain - true stress curves of the present alloys at ST state. The stress level of the plastic flow curves clearly increases with Zr addition, highlighting the notable solid solution strengthening contribution of Zr element in the Ti-12Mo-*x*Zr system. In particular, the yield stress of Ti-12Mo-10Zr alloy approaches about 740 MPa, which is notably high for a strain-transformable

Ti-alloy. Likewise, the uniform elongation of all three alloys is higher than ε = 0.24, displaying large ductility. It is worth noting that the plateau-like platform can be observed at the very beginning of plastic deformation in Ti-12Mo-3Zr alloy (marked in Fig. 2). Sun et al. [6] suggested that the appearance of the plateau is related to the strain-induced martensitic transformation. Aiming at clarifying the evolution of strain-hardening behavior, the corresponding strain-hardening rate (dσ/dε) curves of the three alloys are shown in inset of Fig. 2. The three alloys exhibit different types of evolution of the strain-hardening rate. The strain-hardening rate curves are non-monotonic, similar to those observed in TRIP/TWIP β Ti-alloys [6-9, 14]. It can be observed that Ti-12Mo-6Zr displays a noticeable difference with respect to the other two alloys, regarding the presence of a stable strain-hardening rate at about 1750 MPa in the range of ε=0.05-0.13. The underlying mechanisms are investigated in detail by in-situ EBSD and TEM techniques.

3.3 Deformed microstructure characterization

3.3.1 XRD profiles

Fig. 3 shows the XRD profile of Ti-12Mo-*x*Zr (*x*=3, 6, 10) fractured samples. The residual SIM α″ phase can be detected in the Ti-12Mo-3Zr and Ti-12Mo-6Zr alloys. The appearance of residual α″ is related to the occurrence of SIM α″ in the plastic deformation stage in Ti-12Mo-3Zr and Ti-12Mo-6Zr alloys, partially preserved in the alloys after unloading. Such similar phenomenon is also observed in Ti-12Mo alloy [6, 25] and Ti-9Mo-6W alloy [7]. In contrast, only β phase is detected in Ti-12Mo-10Zr alloy without SIM α″, suggesting either SIM α″ did not occur or has completely reversed to β phase during unloading [11].

3.3.2 In-situ EBSD analysis

In order to clarify the activation and the evolution of the TRIP/TWIP microstructure of the present alloys, in-situ EBSD mapping under tension is performed in the early deformation stage. Fig. 4 shows the EBSD analysis of Ti-12Mo-3Zr sample taken from the same region at different strain. The inverse pole figure (IPF) map at ε=0.02 in Fig. 4(a) shows that plate-like deformation bands with different orientations (coded by color contrast) appear in the β grain, upon loading. The green plate-like deformation bands are identified to be SIM α″, as indicated in the corresponding α″ phase maps (Fig. 4(b)). For further clarifications, as shown in Figure 4c, the orientation relationship between green SIM α″ deformation bands and β matrix has been analyzed and found to be in

agreement with the classic crystallographic orientation relationship {211}β //{110}α″ , suggesting that SIM α″ could likely originate directly from the β matrix. It can be seen from Fig. 4(b) that the quantity and thickness of SIM α″ bands (inside Grain A) increase upon loading from ε=0.02 to 0.04. After unloading from ε=0.04, most of the SIM α″ bands are preserved in β matrix. Similar to the observations reported in superelastic Ti-27at.%Nb [26] and TRIP/TWIP Ti-V-Cr-Al [14], internal twinning of SIM α″ as it is observed that the color contrast of some α″ bands become blue upon loading (ε=0.04 loading) and then transformed back to green during unload (ε=0.04 unloading). The α″ twinning mode is identified as {130} $<310>_{\alpha''}$ martensite twinning by crystallographic stereo projection analysis in Fig. 4(c).

Fig. 5 shows in-situ EBSD mapping of Ti-12Mo-6Zr sample. Both {332} <113> twinning (hereafter called as 332T) and SIM α″ can be observed in the deformed sample. The IPF maps in Fig. 5(a) shows that plate-like deformation bands with two different color contrasts (purple and blue) appear in the β matrix. It can be seen from Fig. 5(c) that the first deformation band appears at loading to ε=0.02. A quick multiplication of the bands happens when increasing the tensile strain to ε=0.04. Most of the bands can be indexed as β phase respecting strictly the 332T relationship with respect to the β matrix, confirmed by the stereo projection analysis (Fig. 5(c)). Two variants of 332T can be observed in the grain traced by in-situ EBSD, belonging to two different 332 planes of the matrix (the two common poles circled in Fig. 5(c)). As shown in Fig. 5(a), the two variants of 332T keep unchanged in their crystal orientations and thicknesses after unloading (ε=0.04 unloading), which suggests that the mechanical twinning between the β matrix and 332T is irreversible. In addition, SIM α″ is also formed in the untwinned area of the β matrix, shown in green in the Image Quality (IQ) map in Fig. 5(b). The orientation relationship of SIM α″ with β matrix is {211}β //{110}α″ according to the analysis of stereographic projection pole in Fig. 5(c), indicating that SIM α″ should originate directly from the β matrix. Similar to the observation in unloaded Ti-12Mo-3Zr alloy, the length and thickness of the SIM α″ decrease after unloading from ε = 0.04, meaning that the martensitic transformation β → α″ should be partially reversible.

In a similar way, in-situ EBSD observations are also performed in the Ti-12Mo-10Zr sample, as shown in Fig. 6. The multiplication of deformation bands, identified as 332T by stereographic projection (Fig. 6(c)), can be observed in the β matrix in the IPF map (Fig. 6(a)) during tensile loading. The SIM α″ is not detected during the *in-situ* loading-unloading (Fig. 6(b)), being in coincidence with the absence of SIM α″ in the post-mortem XRD profile (Fig. 3). It suggests that

the SIM α″ is fully suppressed in Ti-12Mo-10Zr sample.

3.3.3 TEM observations

Fig. 7(a) and (b) show the morphology of SIM α" in the deformed Ti-12Mo-3Zr sample by TEM bright-field (BF) and dark-field (DF) images, respectively. It can be seen that a set of SIM α" plates with different orientations appears in the β matrix. The SIM α" plates are, as well, observed in the Ti-12Mo-6Zr sample. Fig. 7(c) and (d) shows a set of parallel SIM α" plates (width < 100 nm) occur in the β matrix between two 332T bands, which is consistent with the in-situ EBSD observations (Fig. 5). In contrast, no SIM α" is observed at TEM length scale in Ti-12Mo-10Zr sample, complementary to the EBSD mapping resolution limited at micrometric scale. The dislocation slip bands are also observed in the BF images of Ti-12Mo-6Zr and Ti-12Mo-10Zr, which can be seen as band-like contrasts in the untwinned β matrix (marked in Fig. 7(c) and (e), respectively). The contrast is due to the inclination of the thin slip bands with respect to the imaging zone axis, resulting in parallel bands cut by the TEM foil surfaces. It is noted in Fig. 7(e) that secondary deformation bands take place inside the primary 332T bands, which is identified by SAED (inset of Fig. 7(f)) as secondary 332T (2^{nd} 332T). The trace of the 2^{nd} 332T plane is almost parallel to the slip bands. It is thought that such coincidence could be related to the accommodation of the stress-strain concentration at primary 332T boundary, when assuming that this twin boundary acts as strong barrier to the intersecting dislocation slip. Aiming at clarify the situation, the Ti-12Mo-6Zr and Ti-12Mo-10Zr foils are re-tilted to <111> zone axis to study the dislocation pile-ups in the β matrix near 332T boundary.

Evidence is presented in Fig. 8, displaying the situation of the dislocation pile-up at a 332T twin boundary in an intersecting slip band. An array of different sets of dislocation lines is observed aligned towards the 332T interface. A gradient of the inter-distance between every two lines can be seen decreasing when approaching the twin boundary. The burgers vectors of the dislocation lines is analyzed by using the three g.b=0 extinction conditions around [111]β zone axis (Fig. 8(b)-(d)). It can be seen a set of dislocation lines is composed by a group of screw dislocations attributed to three Burgers vectors $b=a/2<111>$ (labeled by b1, b2 and b3 in the Fig. 8(a)). The b1 dislocations are aligned and piled up well against the 332T interface (Fig. 8(c)), tangled by the dislocations of the other two burgers vectors, showing complex interactions between piled-up dislocations lines and the gliding dislocations on other slip planes. The additional TEM observation is also performed

at SIM α" boundary in the Ti-12Mo-6Zr foil. It seems that a dislocation transmission from incoming slip band to the interior of SIM α" occurs at the intersection of the two bands. (Supplementary Fig. S1).

4. Discussion

Based on the in-situ EBSD analysis and TEM observations, Fig. 9 shows a global schematic illustration about the evolutions of the deformation microstructure as a function of Zr concentrations. The initial structures of the three alloys at ST state are the equiaxed β grains. And the SIM α″and/or twins could be activated after yielding. As described in Fig. 9(a), the SIM α″ appears just after yielding in Ti-12Mo-3Zr sample, and then {130}<310>α″ twinning forms inside the SIM α″. However, the 332T is not activated all along the loading and unloading process. The mechanical stability in the metastable Ti-alloys is close related to the deformation products, since the required fault energy in activating the deformation modes follows the order: SIM α″ < 332T < 112T < dislocation slip [27]. Therefore, the absence of 332T suggests that the critical resolved shear stress (CRSS) of SIM α″ is lower than that of 332T, due to the "low" beta stability of Ti-12Mo-3Zr. By increasing Zr content to 6%, the 332T is activated prior to SIM α″, presenting a combined TWIP+TRIP deformation mechanism. Further increasing of Zr content to 10%, the SIM α″ is fully suppressed during the loading-unloading process. It can be seen that the fine-tuning of deformation mechanism, from single TRIP via combined TRIP+TWIP to single TWIP, is achieved by progressively increasing the Zr content in Ti-12Mo-xZr alloy. Nevertheless, it has to be noted that the Mo_{eq} estimation of Zr fails to predict the mechanical stability of Ti-12Mo-xZr. According to the activation of deformation mechanisms at room temperature, the mechanical stability order of the three alloys at ST state should be proposed as: Ti-12Mo-3Zr < Ti-12Mo ≈ Ti-12Mo-6Zr < Ti-12Mo-10Zr. The result suggests that the Zr effect on the chemical stability in metastable Ti-alloys is not linear as proposed in the Mo_{eq} estimation, especially at the low concentration range Zr % < 6%. It has been reported that the Zr addition can achieve dual effects in Ti-Nb based alloys. One is the compositional effect, namely, Zr addition could decrease Ms temperature, so that suppress the martensitic transformation from the β phase to SIM α″ [28]. The other one is the suppression effect of ω formation for SIM α″ [24]. Al-Zain et al. [29] has observed that the ω_{ath} phase can suppress the SIM α″ in Ti-Nb-Mo alloys, implying that the weaker ω precipitation could increase M_s temperature. Therefore, the mechanical stability of Ti-12Mo-*x*Zr alloys could depend on the dual effects of Zr addition. The Zr content up to 3% in Ti-12Mo-*x*Zr suggests that the effect

of Zr on the suppression of ω_{ath} phase is stronger than the compositional effect. The addition of Zr leads to a lower mechanical stability in Ti-12Mo-3Zr than that in Ti-12Mo. With the increase of Zr content (from 3% to 10%), the effect of suppressing ω phase become weaker and the compositional effect becomes dominant. Therefore, the mechanical stability of Ti-12Mo-*x*Zr (x = 3, 6, 10) increases with the Zr addition. The phenomena are similar with the Sn content on Ti-Nb-Mo-based alloys [30, 31] and the Ta content on Ti-Nb based alloys [32].

Regarding the mechanical behavior, the three alloys display remarkable differences in their yield stress, uniform elongation and strain-hardenability. The yield stress could be described to the synergetic co-operations among the grain-size strengthening, the Zr solution hardening and the CRSS of SIM α″ and/or 332T. The average grain-sizes of the three alloys are measured to be about 100 μm, implying that the grain-size provides an almost equal contribution to the yield stress. The effect of the Zr solution hardening is proportional to its content in the multi-component Ti-alloys [33]. In addition, regarding the fault energy order mentioned in the above discussion section, a reasonable presumption is the CRSS of SIM α″ should be lower than that of 332T. Thus, plausible explanation can be suggested about the evolution of the yield stress in both Ti-12Mo-3Zr and Ti-12Mo-10Zr alloys from 520MPa to 740MPa. However, it seems that the evolution of the yield stress is less than expected in Ti-12Mo-3Zr and Ti-12Mo-6Zr alloys (from 520MPa to only 590MPa). In other words, the evolution of yield stress seems to be non-linear. The phenomenon probably originates from two-fold factors: 1) the weakening of ω_{ath} precipitation hardening effect, due to the ω_{ath} phase decrease with the increasing Zr content in Ti-12Mo-xZr alloys; 2) the formation of SIM α″ in Ti-12Mo-6Zr also could be responsible for the limited yield stress. The SIM α″, although observed with low area fraction in some grains (Fig. 5), could still be active enough in other grains orientated favorably to SIM α″, leading to a heterogeneous yielding process. The grains favored SIM α″ could initiate martensitic transformation before the twin nucleation and growth in the grains favored 332T, resulting in an earlier yielding than expected. The similar mechanism has been also reported in the TRIP/TWIP Ti-12Mo [6] and Ti-V-Cr-Al [14] alloys.

Additionally, the three alloys with large uniform elongation show an individual evolution of strain-hardening rate. The large uniform elongation corresponds to enough strain-hardenability, suggesting delay the occurrence of necking [34]. The Ti-12Mo-6Zr alloy shows the highest strain-hardening rate when compared with Ti-12Mo-3Zr and Ti-12Mo-10Zr. The difference in strain-hardening rates could result from the various evolution of deformation microstructure. The

deformation microstructure evolution in Ti-12Mo-*x*Zr alloys indicates deformation pathways between the two deformation modes (TRIP and TWIP) as a function of the progressive increase of Zr addition. In other words, the tuning of the deformation mechanisms could be realized by fine-tuning Zr content. Regarding the comparison of the strain-hardening behavior among the TWIP alloys, the back-stress due to the dislocation pile-ups at boundary/slip band intersections can be considered as the key factor responsible for the kinematic hardening [10]. By TEM investigations, the occurrence of dislocation pile-ups is confirmed near the matrix/332T and matrix/SIM α″ boundaries (shown in Fig. 8 and S1). Usually the dislocation pile-ups in these interfaces could cause the back-stress fields. And the stress fields provide a long-range strengthening effect throughout the plastic deformation. Qualitatively, the back-stress is usually evaluated to be linearly proportional to the inverse of the mean inter-boundary spacing, i.e. the distance between two adjacent boundaries of the deformation bands (SIM α″ and/or 332T) [35]. Since the thickness of the bands observed in the three alloys are quite similar, the inverse of the mean inter-boundary spacing is therefore governed by the transformed or twinned fraction of the alloy at a given strain. The kinetic of the nucleation and growth of the deformation bands has been studied by Olson and Cohen [36] for SIM α″ nucleation, and the same model has been adopted by Bouaziz [37] for twinning. The kinetic model has been applied successfully to describe the stress-strain behavior in single TWIP Ti-alloys [10]. Indeed, The strain-hardening behavior of Ti-12Mo-10Zr is consistent with the literature modelling results [10] since the deformation mechanism operated is single TWIP, compatible with the simple shear band assumption used in Olson and Cohen kinetic model. However, in the case of Ti-12Mo-6Zr with mixed TRIP/TWIP mechanisms, the same kinetic TWIP model is not well supported by the experimental results. The Ti-12Mo-6Zr presents a much higher strain-hardening rate than the other two alloys after the yield point (Fig. 2). It is thought that the difference of strain-hardening rate could be related to the localized SIM α″formation in the untwinned β matrix, which is not considered in the current kinetic model. It can be seen from the EBSD and TEM images that short SIM α″ bands are likely to form in the untwinned β matrix between two adjacent twin boundaries. Their formation could be due to the accommodation of the highly localized stress or strain misfits near the twin boundaries and grain boundaries. Similar situations have been reported in Ti-V-Cr-Al alloy [14] and Ti-Mo-W alloy [7]. Then it is quite obvious evident that these local SIM α″ bands further increase the total volume fraction of deformation products than predicted by Olson and Cohen model, and therefore further reduce the inter-spacing of the

deformation-induced boundaries in the β matrix (illustrated schematically in Fig. 9). This special fact in the microstructure evolution combing TRIP and TWIP may be one of the reasons to explain the high strain-hardening rate of Ti-12Mo-6Zr when comparing to Ti-12Mo-10Zr. As for Ti-12Mo-3Zr, the strain-hardening behavior at early deformation stage ($\varepsilon<0.05$) is very similar with that of Ti-12Mo-10Zr. The finding is corroborated by the similar microstructure evolutions observed in the two alloys. It might suggest that the Olson and Cohen's kinetic could be valid to describe the nucleation and growth of SIM α″ at the early stage of the plastic deformation in TRIP Ti-alloys. However, in the late stage, the strain-hardening rate increases rapidly to the level close to the strain-hardening rate of Ti-12Mo-6Zr, which means the increasing strain-hardening rate can be due to other reasons. The exact mechanism requires further investigations.

5. Conclusions

In this work, the influence of Zr element on microstructure evolution, mechanical properties and deformation mechanism of the Ti-12Mo-xZr (x=3, 6, 10) alloys are investigated. The following main results are obtained.

(1) The transition from TRIP effect to TWIP effect in the Ti-12Mo-xZr alloys can be realized by fine-tuning the addition of Zr element.

(2) All the three alloys display an excellent strength-ductility. But the yield stress of Ti-12Mo-10Zr alloy which is much higher than that of Ti-12Mo-6Zr and Ti-12Mo-3Zr, coming from the absence of SIM during deformation, as well as solid solution strengthen of Zr element.

(3) Ti-12Mo-6Zr alloys display a higher strain-hardening rate when compared to Ti-12Mo-3Zr and Ti-12Mo-10Zr, which resulted from a mixture of both TRIP and TWIP mechanisms.

Acknowledgments

The work was supported by National Natural Science foundation of China (Grant No. 51601216 and 51901193); China Postdoctoral Science Foundation (Grant No. 2018M632414); Fund of State Key Lab of Advanced Metals and Materials, University of Science and Technology Beijing (Grant No.2019-ZD03), Fundamental Research Funds for the Central Universities (Grant No. 2017XKQY009), Funds of Industry-University-Research Cooperation in Jiangsu Province (Grand No.BY2018075) and Key Research and Development Program of Shaanxi (Grant No. 2019GY-151). Mr. Bingnan QIAN is sponsored by China Scholarship Council.

References

[1] J.C. Williams, E.A. Starke Jr., Acta Mater. 51 (2003) 5775-5799.

[2] M.J. Xiao, Y.X. Tian, G.W. Mao, S.J. Li, Y.L. Hao, R. Yang, J. Mater. Sci. Technol. 27 (2011) 1099-1104.

[3] Y. Huang, Y. Liu, C. Li, Z. Ma, L. Yu, H. Li, Vaccum 161 (2019) 209-219.

[4] S. Yan, G.-L. Song, Z. Li, H. Wang, D. Zheng, F. Cao, M. Horynova, M.S. Dargusch, L. Zhou, J. Mater. Sci. Technol. 34 (2018) 421-435.

[5] C. Lan, Y. Wu, L. Guo, H. Chen, F. Chen, J. Mater. Sci. Technol. 34 (2018) 788-792.

[6] F. Sun, J. Zhang, M. Marteleur, T. Gloriant, P. Vermaut, D. Laillé, P. Castany, C. Curfs, P.J. Jacques, F. Prima, Acta Mater. 61 (2013) 6406-6417.

[7] F. Sun, J. Zhang, M. Marteleur, C. Brozek, E.F. Rauch, M. Veron, P. Vermaut, P.J. Jacques, F. Prima, Scr. Mater. 94 (2015) 17-20.

[8] L. Ren, W. Xiao, C. Ma, R. Zheng, L. Zhou, Scr. Mater. 156 (2018) 47-50.

[9] J Zhang, J. Li, G. Chen, L. Liu, Z. Chen, Q. Meng, B. Shen, F. Sun, F. Prima, Mater. Charact. 139 (2018) 421-427.

[10] G.H. Zhao, X. Xu, D. Dye, P.E.J. Rivera-Díaz-del-Castillo, Acta Mater. 183 (2020) 155-164.

[11] J. Zhang, F. Sun, Z. Chen, Y. Yang, B. Shen, J. Li, F. Prima, Mater. Res. Lett. 7 (2019) 251-257.

[12] M.J. Lai, T. Li, D. Raabe, Acta Mater. 151 (2018) 67-77.

[13] S.A. Mantri, F. Sun, D. Choudhuri, T. Alam, B. Gwalani, F. Prima, R. Banerjee, Sci. Rep. 9 (2019) 1334.

[14] L. Lilensten, Y. Danard, C. Brozek, S. Mantri, P. Castany, T. Gloriant, P. Vermaut, F. Sun, R. Banerjee, F. Prima, Acta Mater. 162 (2019) 268-276.

[15] J.Y. Zhang, G.F. Chen, Y.Y. Fu, Y. Fan, Z. Chen, J. Xu, H. Chang, Z.H. Zhang, J. Zhou, Z. Sun, B.L. Shen, F. Sun, J. Alloys Compd. 799 (2019) 389-397.

[16] J. Zhang, Y. Fu, Y. Wu, B. Qian, Z. Chen, A. Inoue, Y. Wu, Y. Yang, F. Sun, J. Li , F. Prima, Mater. Res. Lett. 8 (2020) 247-253.

[17] L.C. Zhang, T. Zhou, S.P. Alpay, M. Aindow, M.H. Wu, Appl. Phys. Lett. 87 (2005) 241909.

[18] R. Davis, H.M. Flower, D.R.F. West, J. Mater. Sci. 14 (1979) 712-722.

[19] M. Hida, E. Sukedai, C. Henmi, K. Sakaue, H. Terauchi, Acta Metall. 30 (1982) 1471-1479.

[20] X. Min, X. Chen, S. Emura, K. Tsuchiya, Scr. Mater. 69 (2013) 393-396.

[21] J.Y. Zhang, F. Sun, Y.L. Hao, N. Gozdecki, E. Lebrun, P. Vermaut, R. Portier, T. Gloriant, P. Laheurte, F. Prima, Mater. Sci. Eng. A 563 (2013) 78-85.

[22] M. Abdel-Hady, H. Fuwa, K. Hinoshita, H. Kimura, Y. Shinzato, M. Morinaga, Scr. Mater. 57 (2007) 1000-1003.

[23] Q. Wang, C. Dong, P.K. Liaw, Metall. Trans. A 46 (2015) 3440-3447.

[24] E.L. Pang, E.J. Pickering, S.I. Baik, D.N. Seidman, N.G. Jones, Acta Mater. 153 (2018) 62-70.

[25] J.Y. Zhang, J.S. Li, Z. Chen, Q.K. Meng, F. Sun, B.L. Shen, J. Alloys Compd. 699 (2017) 775-782.

[26] P. Castany, Y. Yang, E. Bertrand, T. Gloriant, Phys. Rev. Lett. 117 (2016) 245501.

[27] X.Y. Zhou, X.H. Min, S. Emura, K. Tsuchiya, Mater. Sci. Eng. A 684 (2017) 456-465.

[28] Y.L. Hao, S.J. Li, S.Y. Sun, R. Yang, Mater. Sci. Eng. A 441 (2006) 112-118.

[29] Y. Al-Zain, H.Y. Kim, H. Hosoda, T.H. Nam, S. Miyazaki, Acta Mater. 58 (2010) 4212-4223.

[30] D.C. Zhang, S. Yang, M. Wei, Y.F. Mao, C.G. Tan, J.G. Lin, J. Mech. Behav. Biomed. Mater. 13 (2012) 156-165.

[31] M.F. Ijaz, H.Y. Kim, H. Hosoda, S. Miyazaki, Scr. Mater. 72 (2014) 29-32.

[32] H.Y. Kim, S. Hashimoto, J.I. Kim, T. Inamura, H. Hosoda, S. Miyazaki, Mater. Sci. Eng. A 417 (2006) 120-128.

[33] G.H. Zhao, X.Z. Liang, B. Kim, P.E.J. Rivera-Díaz-del-Castillo, Mater. Sci. Eng. A 756 (2019) 156-160.

[34] A.K. Ghosh, Acta Metall. 25 (1977) 1413-1424.

[35] Q. Luo, Y. Guo, B. Liu, Y. Feng, J. Zhang, Q. Li, K. Chou, J. Mater. Sci. Technol. 44 (2020) 171-190.

[36] G.B. Olson, M. Cohen, Metall. Trans. A 6 (1975) 791.

[37] O. Bouaziz, N. Guelton, Mater. Sci. Eng. A 319 (2001) 246-249.

Figure list:

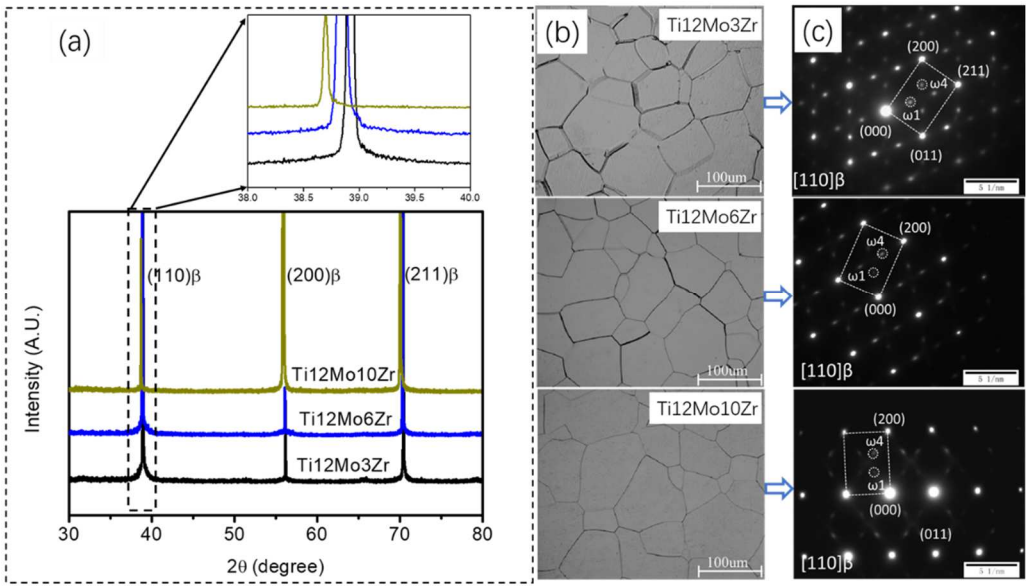

Fig. 1. Characterizations of the Ti-12Mo-*x*Zr (*x*=3, 6, 10) alloys at ST state. (a) XRD profiles; (b) Optical images; (c) SAED patterns along the [110]β zone axis. The peak position of (110)β of the three alloys is magnified in inset of (a). Two of the four ω-variants, labelled ω1 and ω4, are also discriminated on the basis of the reflections in (c).

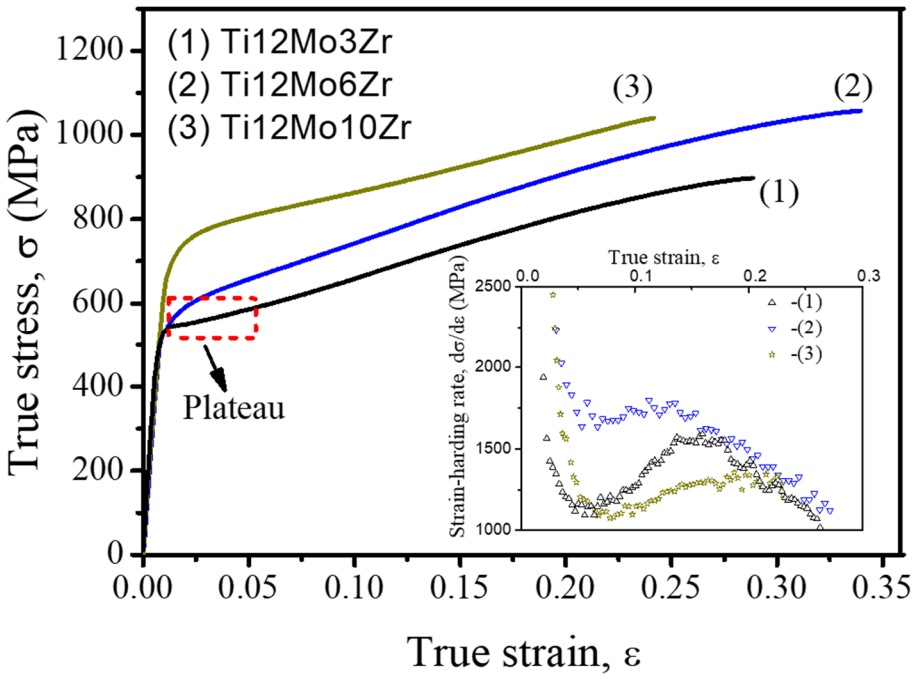

Fig. 2. True strain-stress curves of the ST Ti-12Mo-*x*Zr (*x*= 3, 6, 10) samples, and the corresponding strain-hardening rate curves as function of true strain also shown in inset.

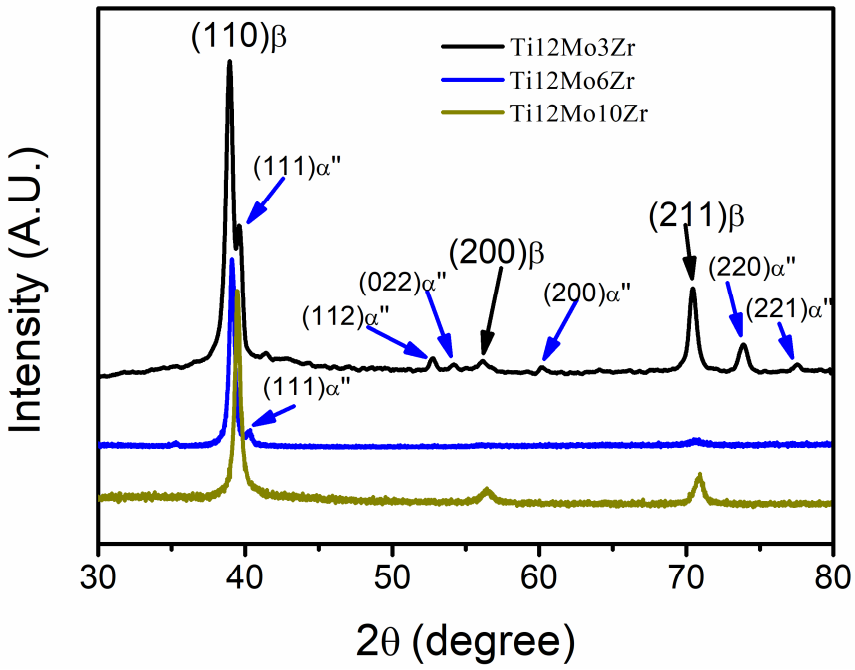

Fig. 3. XRD profiles of the ST sample of Ti-12Mo-*x*Zr (*x*= 3, 6, 10) alloys after deformation until fracture.

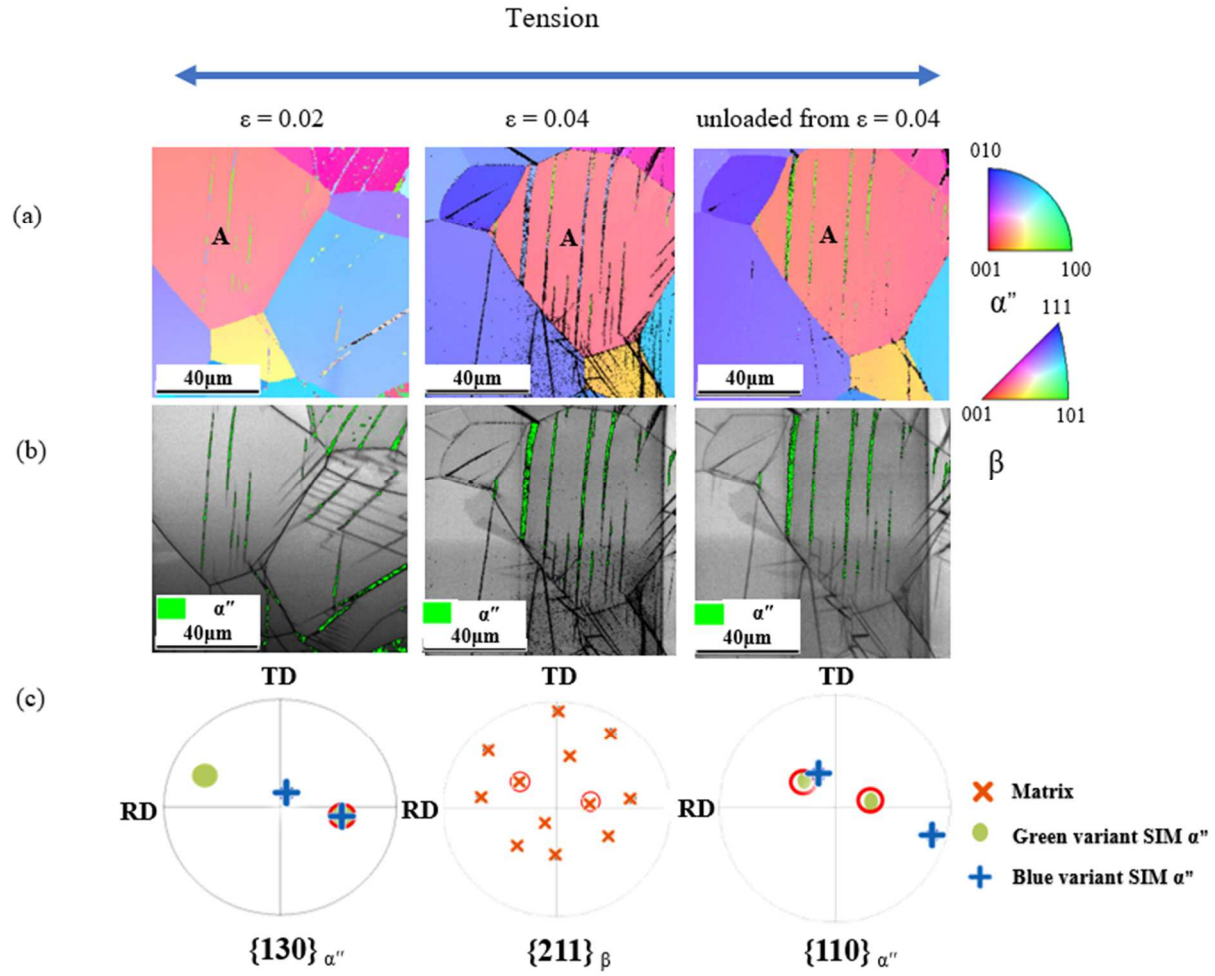

Fig. 4. EBSD analysis of the Ti-12Mo-3Zr deformed sample taken from the same region at strain ε=0.02 (loading), 0.04 (loading), and 0.04 (unloading), respectively. (a) IPF maps; (b) orientation maps for SIM α″ phase; (c) pole figures of β matrix and SIM α″. (RD – rolling direction, TD – transverse direction).

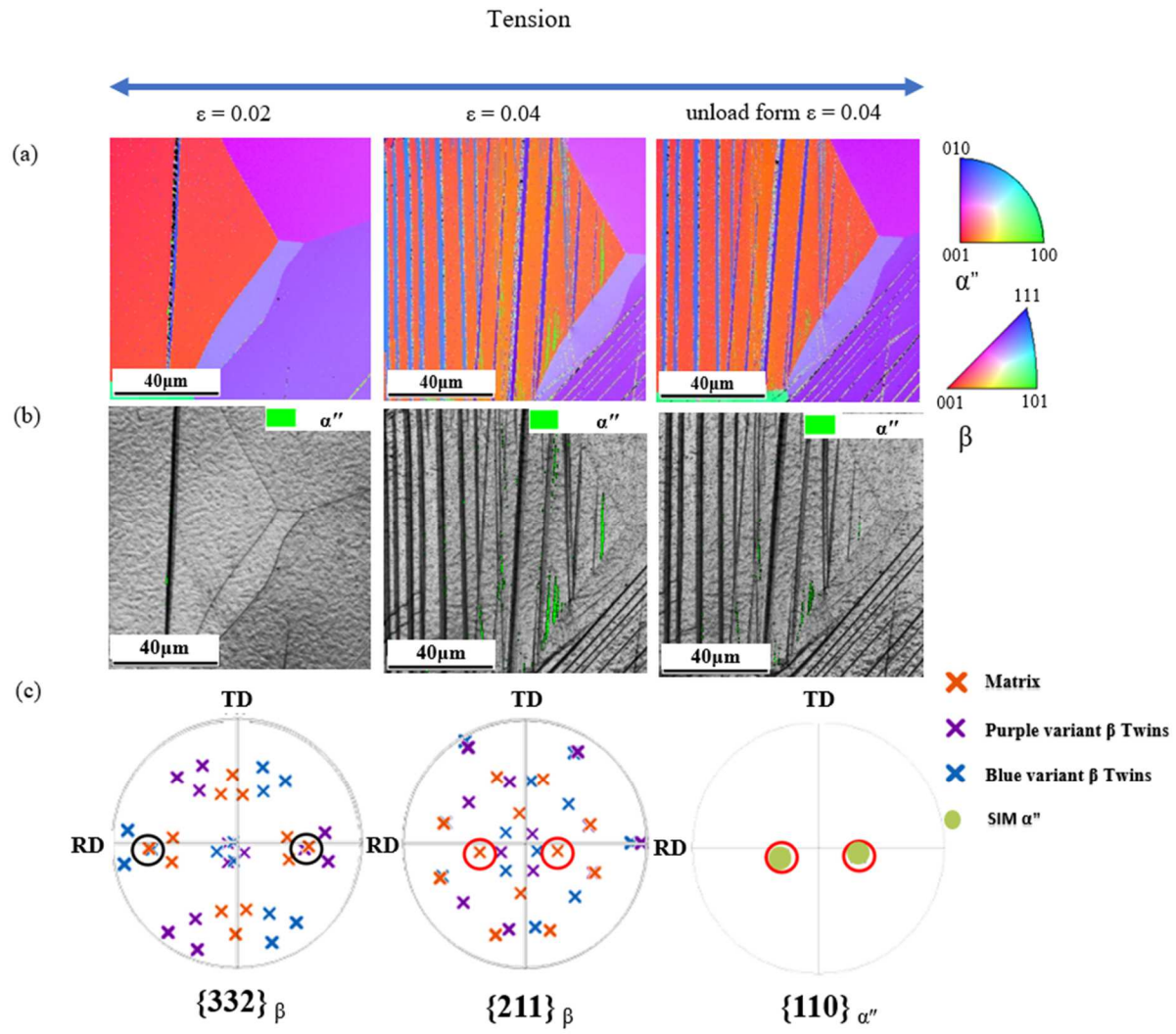

Fig. 5. EBSD analysis of the Ti-12Mo-6Zr (Type A) deformed sample taken from the same region at strain ε=0.02 (loading), ε=0.04 (loading), and 0.04 (unloading), respectively. (a) IPF maps; (b) orientation maps for α″ phase; (c) pole figures of β matrix, {332}<113> twinning and SIM α″. (RD – rolling direction, TD – transverse direction).

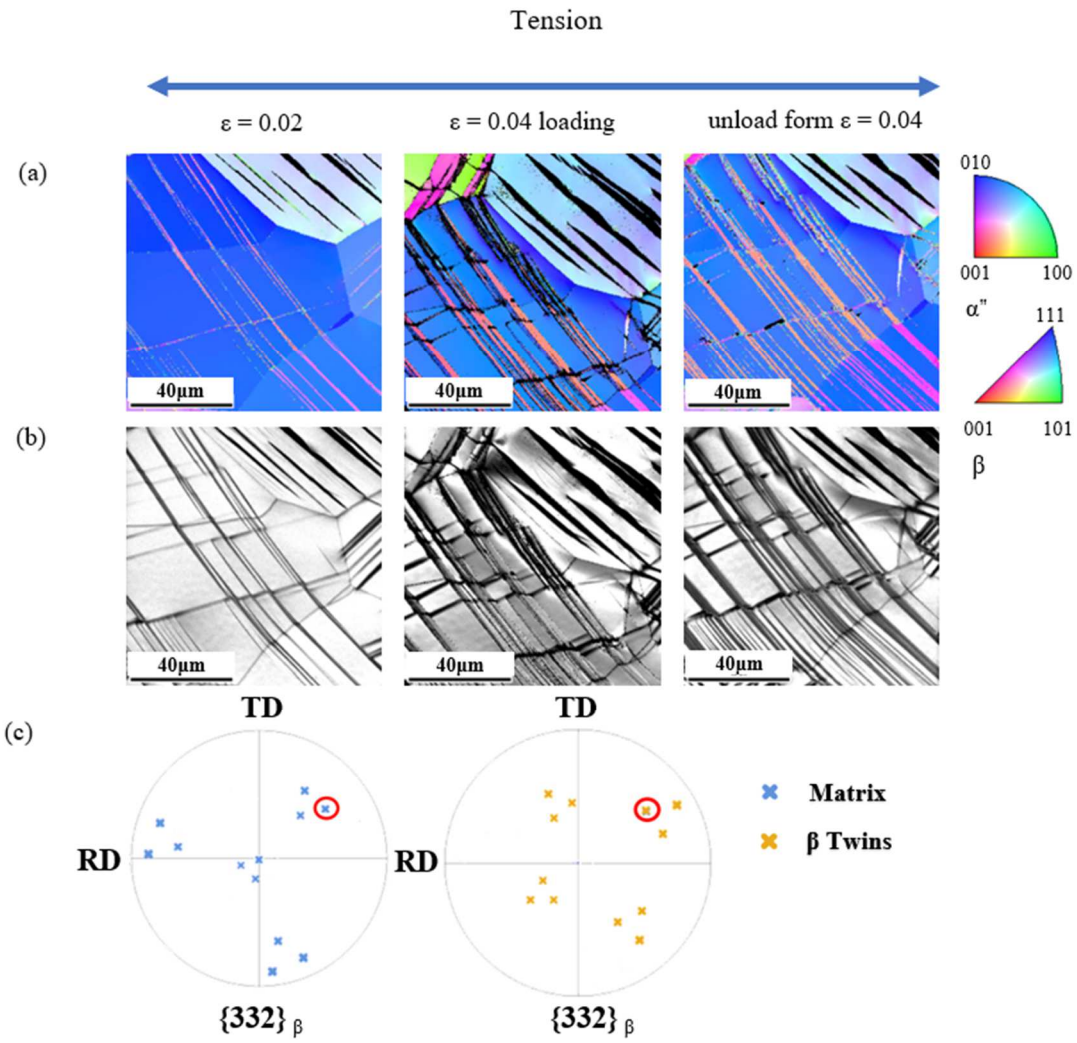

Fig. 6. EBSD analysis of the Ti-12Mo-10Zr deformed sample taken from the same region at strain ε=0.02 (loading), 0.04 (loading), and 0.04 (unloading), respectively. (a) IPF maps; (b) orientation maps for α″ phase; (c) pole figures of β matrix, {332}<113> twinning. (RD – rolling direction, TD – transverse direction).

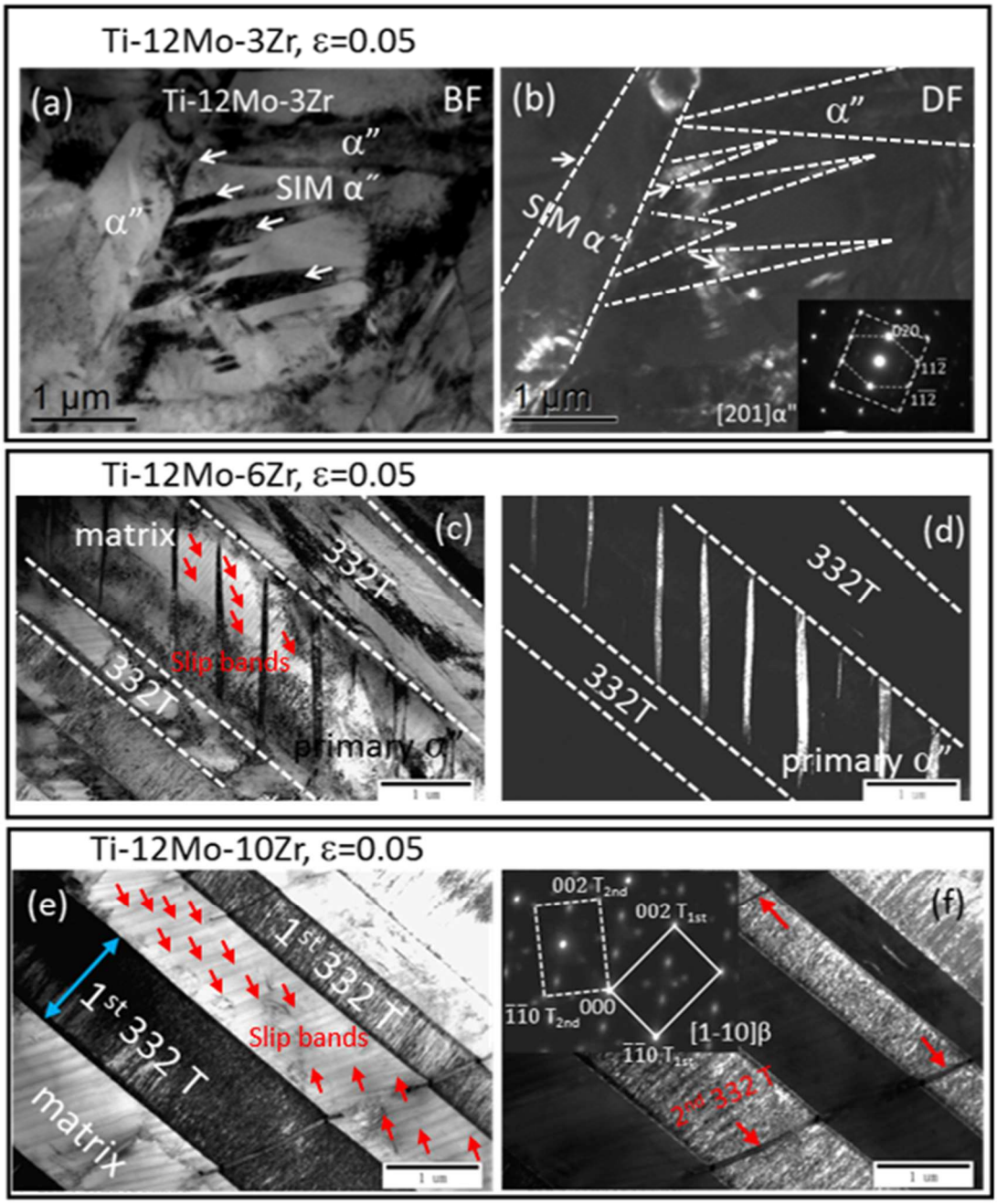

Fig. 7. TEM micrographs of Ti-Mo-Zr samples after tensile deformation to ε=0.05: (a) bright-field (BF) image of the Ti-12Mo-3Zr showing SIM α" bands; (b) dark-field (DF) image of one variant of the SIM α" in (a); (c) BF image of the Ti-12Mo-6Zr showing primary 332T bands and the primary SIM α"; (d) DF image of the primary SIM α" in (c); (e) BF image of the Ti-12Mo-10Zr showing primary 332T bands with secondary 332T bands; (f) DF image of (e) with the corresponding SAED pattern along [1-10]β zone axis.

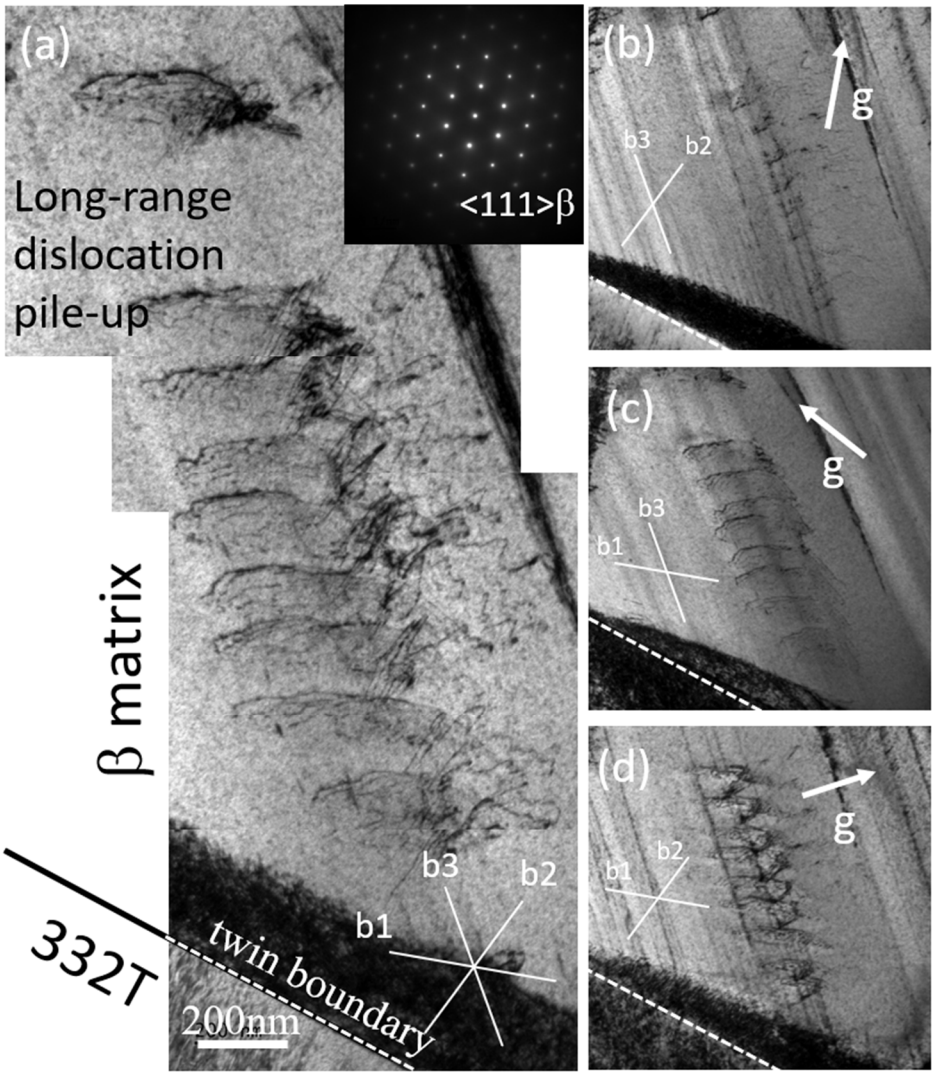

Fig. 8. TEM micrographs of Ti-12Mo-6Zr at ε=0.05: (a) BF image of an array of dislocations piled up to the 332T interface; (b-d) BF images of the three g conditions around [111] β zone axis.

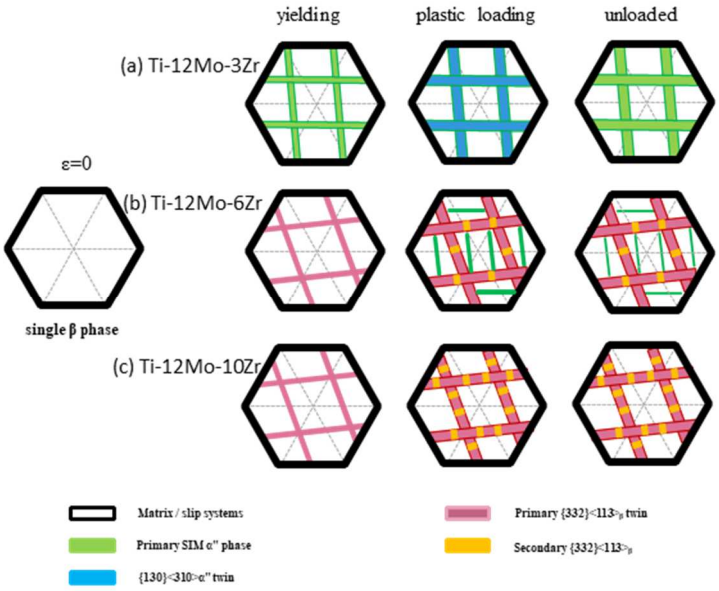

Fig. 9. Schematic formation sequence of 332T and SIM α″ during loading and unloading process in (a) Ti-12Mo-3Zr; (b) Ti-12Mo-6Zr and (c) Ti-12Mo-10Zr alloys.